Active Acoustic Su-Schrieffer-Heeger-Like Metamaterial

Mathieu Padlewski,[1,*] Maxime Volery,[1] Romain Fleury,[2] Hervé Lissek,[1] and Xinxin Guo[1]

[1] *Signal Processing Laboratory 2, EPFL 1015 Lausanne, Switzerland*

[2] *Laboratory of Wave Engineering, EPFL, 1015 Lausanne, Switzerland*

(Received 21 February 2023; revised 4 May 2023; accepted 7 June 2023; published 12 July 2023)

An acoustic dimer composed of two electronically controlled electroacoustic resonators is presented with the view of exploring one-dimensional topological phenomena. Active control allows real-time manipulation of the metamaterial's properties, including its mechanical mass, resistance, compliance, and internal coupling. The latter enables active tuning of the topological phase transition in the effective acoustic Su-Schrieffer-Heeger system. An analytical model of the unit cell as well as the electronic control scheme is provided. Band structures derived from the analytical model, the finite-element simulation, and the experimental data consistently demonstrate the realization of a tunable one-dimensional topological insulator.

DOI: 10.1103/PhysRevApplied.20.014022

I. INTRODUCTION

The study of collective wave phenomena in condensed-matter physics and photonics has proven to be an essential asset for the development of pioneering technologies that have shaped the modern world—transistors, photovoltaics, and charge-coupled devices to name a few. A notable drawback for these fields of research, however, is the often-highly-complex and costly equipment required to observe microscopic phenomena occurring at the quantum scale. One solution would be to increase the scale of the physics being studied and to observe wave phenomena in macroscopic crystalline structures.

Acoustic metamaterials (AMMs) are materials that can be engineered to exhibit properties similar to those found in quantum systems and even *beyond* the realm of naturally occurring materials. In addition to their complexity and cost, macroscopic wave systems have notable advantages over those at the quantum scale. The salient physics of quantum systems, for example, is well defined in theory, but lacks atomic probes capable of readily determining eigenvalues and directly measuring eigenfunctions. On the other hand, classical analogues of these systems can offer complete observability and control of these quantities [1,2]. Generally speaking, AMMs can provide valuable insight into systems where theoretical calculations are not easily tractable, even with modern computers, particularly systems involving time-dependent potential fields, disorder, or nonlinearity.

Topological insulators are a highly attractive area of research in condensed-matter physics owing to features such as robust solitons or interface states. Unfortunately, progress in this field is greatly hindered by the limited number of available crystal candidates exhibiting such properties and the difficulty to perform experiments. Conversely, many analogous acoustic systems demonstrating topological regimes have been studied owing to the relative ease with which experimental fabrication and measurement are done [3–9]. For example, Zhao *et al.* [10] proposed an acoustic duct lined with Helmholtz resonators where a linear intersite coupling is fixed by spatial separation between subsequent pairs with the view of understanding topology within a locally resonant band gap. Effective controllability, tunability, and reconfigurability remain desirable properties that are unfortunately beyond the scope of these passive systems.

The emerging field of active acoustic systems, on the other hand, could provide phase-transition and soliton-formation manipulation through the application of active control schemes allowing the exploration of new exotic phenomena. It is clear that advances in non-Hermitian *PT*-symmetric [11–16], dynamically reconfigurable [17], and nonreciprocal [18–23] systems and real-time manipulation of the effective acoustic properties [24,25] provide the necessary tools for seeking new topological phenomena.

The active electroacoustic resonator (AER) allows the achievement of prescribed frequency-dependent acoustic impedances at the acoustic interface of an electroacoustic transducer such as a loudspeaker [26]. Such devices have been shown to successfully achieve tunable sound absorption [27,28]. They have also been used as active unit cells in a non-Hermitian acoustic medium [29] and in an active acoustic metasurface concept for shaping reflected wave fronts in a controllable manner [30].

*mathieu.padlewski@gmail.com

This study presents an actively tunable AMM capable of exhibiting prescribed topological features similar to those found in the Su-Schrieffer-Heeger (SSH) system [31]—a one-dimensional chain of coupled dimers that can host topological modes owing to its two coupling-dependent regimes. Although successful realizations of this system have been achieved via passive metastructures [32–34], here we demonstrate an actively tunable dimer composed of two electronically controlled AERs. First, an analytical model of the unit cell is presented, followed by the active control scheme used to tune dimerization of the unit cell. Fidelity of the model is demonstrated by our comparing crystal dispersions obtained for both the model and the experimental unit cell. Using a transfer-matrix approach, we finally demonstrate that the system can host topological edge states via a finite-crystal simulation and that they are protected by both time-reversal symmetry and equality of the far-field scattering matrices.

II. DESCRIPTION OF THE BASELINE SSH-LIKE UNIT-CELL

Suppose we have a crystal unit cell composed of a duct segment loaded with two identical and equally spaced AERs that are fixed in place as shown in Fig. 1(a). A periodic array of these cells paired with coupling would form an SSH-like chain along the x axis. Assuming continuity of pressure and volumetric flow, the transfer matrix M_{cell} relating amplitudes in subsequent cells can be obtained with use of the transfer-matrix method (TMM) [35,36]. The latter depends solely on the cell's geometric properties and the complex mechanical impedances ζ_m of the resonators. The crystal band structure can be obtained by application of the Bloch theorem and by computation of the eigenvalues.

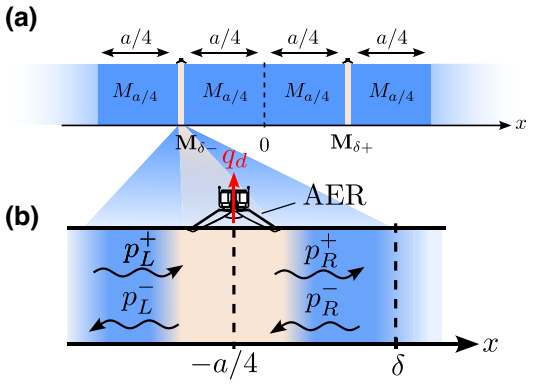

FIG. 1. Transfer-matrix approach to the active acoustic SSH-like unit cell. (a) Unit cell of length a composed of a duct segment loaded with two equally spaced AERs that are fixed in place. It can be split into six segments, each described by its own transfer matrix M. (b) An AER fixed at position $x = -a/4$. δ (the dimerization parameter) is the distance from the AER and is related to the coupling strength (see the main text). Incoming and outgoing complex field amplitudes on both sides of the speaker-plane interface (p_L^+, p_L^-, p_R^+, and p_R^-) are represented by the arrows.

The total single-cell transfer matrix of the active system is simply given by multiplication of the individual transfer matrices of each of its constituents:

$$M_{\text{cell}} = M_{a/4}\mathbf{M}_{\delta-}M_{a/4}M_{a/4}\mathbf{M}_{\delta+}M_{a/4}, \tag{1}$$

where $M_{a/4}$ represents the straight duct of length $L = a/4$ and $\mathbf{M}_{\delta\pm}$ is the transfer matrix through the AER plane with dimerization parameter δ related to the cell coupling strength. We consider the case of the left AER, which is placed flat against the duct wall at position $x = -a/4$ as shown in Fig. 1(b). $\mathbf{M}_{\delta-}$ is computed by our considering the following:

(a) The target *remote* impedance is defined as follows:

$$\tilde{\zeta}_{\delta-} = S_d^2 \times \frac{p(x = -a/4 + \delta)}{q_d}, \tag{2}$$

where S_d, p, and q_d are the effective diaphragm surface area, pressure, and volumetric flow through the diaphragm, respectively. In contrast to the *real* speaker impedance, the evaluated pressure and velocity here are spatially separated by a distance δ.

(b) The pressure radiated from the speaker at any position x in the duct can be written as follows:

$$p_{rs}(x) = -\frac{\rho c q_d}{2S} e^{-ik|x+a/4|}, \tag{3}$$

where ρ, c, S, and k are the air density, the speed of sound in air, the duct cross-section area, and the wave number, respectively.

(c) The volumetric flow conservation and pressure continuity at $x = -a/4$ yields

$$p_R^+ = -\frac{\rho c}{2S} q_d + p_L^+, \tag{4}$$

$$p_L^- = -\frac{\rho c}{2S} q_d + p_R^-, \tag{5}$$

where p_L^+ and p_L^- are the forward and backward complex field amplitudes on the left of the speaker and p_R^+ and p_R^- are the amplitudes on the right of the speaker.

The impedance defined in Eq. (2) is imposed by means of active control at the AER. Using Eqs. (3)–(5), we obtain the transfer matrix for the left AER $\mathbf{M}_{\delta-}$:

$$\begin{pmatrix} p_R^+ \\ p_R^- \end{pmatrix} = \underbrace{\left(\mathbb{1} + w_{\delta-}\begin{pmatrix} e^{-jk\delta} & e^{jk\delta} \\ -e^{-jk\delta} & e^{jk\delta} \end{pmatrix}\right)^{-1}}_{\mathbf{M}_{\delta-}} \begin{pmatrix} p_L^+ \\ p_L^- \end{pmatrix}, \tag{6}$$

where

$$w_{\delta-} = \frac{\rho c S_d^2}{2S\tilde{\zeta}_{\delta-}}.$$

By symmetry of the unit cell, the transfer matrix for the right AER, $M_{\delta+}$, is the same albeit with δ of opposite sign.

Finally, the band structure is obtained with use of Eq. (1) and by application of the Floquet-Bloch theorem, yielding

$$q_F(k) = \arccos\left(\frac{1}{2}Tr(M_{\text{cell}}(k))\right)/a, \tag{7}$$

where q_F is the Floquet-Bloch wave number (details are given in Appendix A).

III. TAILORING THE DISPERSION THROUGH ACTIVE CONTROL

To achieve active impedance control, the experimental unit cell is equipped with microphones placed in front of and in between the lined AERs as shown at the bottom of Fig. 2(b). The system is tuned via an active-feedback control scheme that is split into two parts, each of which aims at altering the gaps present in the dispersion of the coupled resonator metastructure, namely, a band-folding *Bragg gap* and a band-folding *locally resonant gap*, highlighted in Fig. 2(a).

A. Shaping the locally resonant gap

The band-folding *locally resonant gap* results from the coupling of a continuum of propagating waves and a local resonance that can be described by a polariton-like dispersion [37], albeit folded for a doubled unit cell. Its position and size can be shaped at the experimenter's discretion by the experimenter altering the AER's resonance frequency and quality factor [27,30,38]. The desired target mechanical impedance ζ_{st} is specified by the control parameters μ_M, μ_R, and μ_C:

$$\zeta_{st}(s) = \mu_M M_{ms} s + \mu_R R_{ms} + \mu_C / C_{mc} s, \tag{8}$$

where $s = j\omega$ is the Laplace variable, M_{ms} is the diaphragm mass (kg), R_{ms} is the mechanical resistance (kg/s), and C_{mc} is the compliance of the diaphragm and the cabinet (s^2/kg).

ζ_{st} synthesis is achieved by multiplication of the real-time front pressure by a transfer function $\Phi(\zeta_{st})$ [26], resulting in the current required to drive the AERs (details are given in Appendix B).

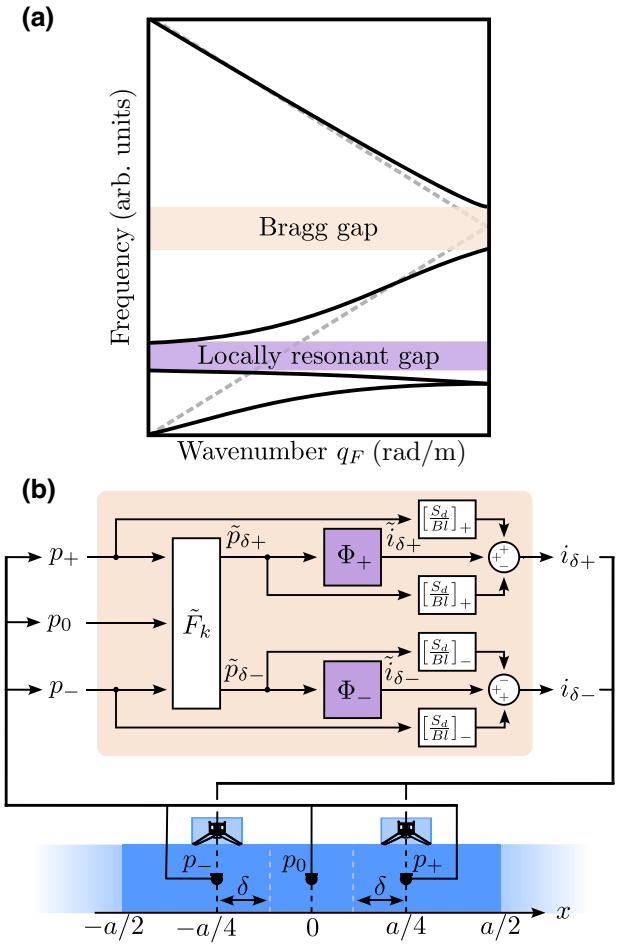

FIG. 2. Active dispersion shaping. (a) Dispersion of a lossless coupled-resonator system with two gaps: a Bragg gap and a locally resonant gap. (b) Block diagram of the proposed control scheme wired to the experimental unit cell. From left to right, the acoustic pressures in front of and in between the AERs (p_+ and p_-, and p_0, respectively) are used as inputs for the $\tilde{F}_k$ function, which serves to achieve the δ shift. The impedance is synthesized with the desired mechanical parameters specified by the transfer functions Φ_+ and Φ_-. The output currents $i_{\delta+}$ and $i_{\delta-}$ are carried to the respective AERs in the unit cell. Black dots in the unit cell represent pressure microphones.

B. Shaping the Bragg gap

The band-folding *Bragg gap* opens when dimerization is introduced in the crystal [31]. Here we show that a gap forms when the coupling is enhanced via active control. Figure 2(b) shows the proposed block diagram of the control scheme. Knowing the operating wave number k in the waveguide, we can estimate the pressure $\tilde{p}_{\delta\pm}$ between an AER and the center microphones using the function

$$\tilde{F}_k(p_\pm, p_0) := \frac{p_\pm \sin(\pm k(a/4 - \delta)) + p_0 \sin(\pm k\delta)}{\sin(\pm ka/4)}, \tag{9}$$

where δ is the dimerization parameter.

The virtual control current required to synthesize a target impedance Z_{st} is expressed as

$$\tilde{i}_{\delta\pm} = \tilde{p}_{\delta\pm}\Phi_{\pm}, \tag{10}$$

where $\Phi_{\pm}$ is the aforementioned transfer function. Notice that Φ appears twice in the control-scheme block diagram as the AERs' mechanical parameters are synthesized separately.

Finally, the control current $i_{\delta\pm}$ used to drive the AERs are given by

$$i_{\delta\pm} = (p_{\pm} - \tilde{p}_{\delta\pm})\left[\frac{S_d}{Bl}\right]_{\pm} + \tilde{i}_{\delta\pm} \tag{11}$$

IV. RESULTS AND DISCUSSION

A. Analytical model

The theoretical dispersion is computed with use of Eq. (1):

$$\cos(q_F(k)a) = \frac{w_{\delta+}w_{\delta-}[\cos(ka) - \cos(k2\delta)] + w_{\delta+}j\,\sin(k(a+\delta)) + w_{\delta-}j\,\sin(k(a-\delta)) + \cos(ka)}{j\,(w_{\delta+}2j\,\sin(k\delta) + 1)(w_{\delta-}2j\,\sin(k\delta) - 1)}. \tag{12}$$

It is plotted for dimerization values $\delta \in (0, +a/4)$ in Fig. 3(a). The locally resonant and Bragg gaps occur at 500 and 690 Hz, respectively. For $\delta = 0$, the Bragg gap is closed as indicated by the vanishing complex part of the Floquet-Bloch wave number q_F. This is not surprising since it corresponds to the dispersion of equally spaced coupled resonators [10]. As δ increases, however, the gap opens as a result of the change of the intracell coupling. Conversely, negative values of δ, corresponding to intercell coupling, yield identical dispersions.

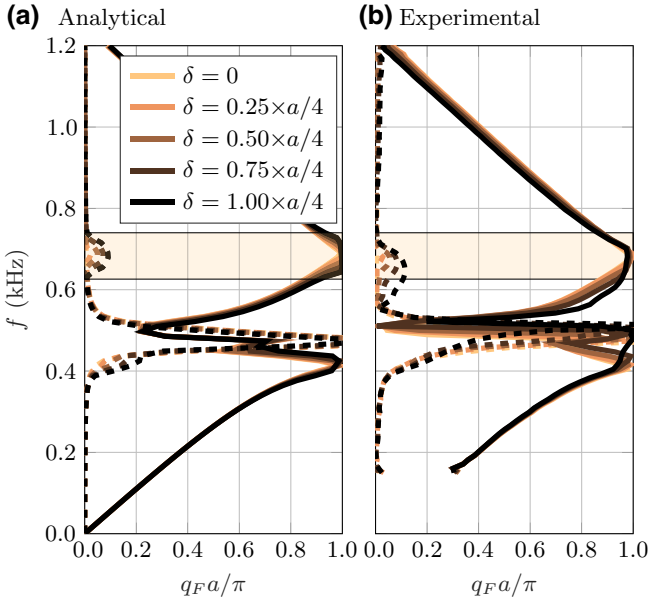

FIG. 3. Active control on the band-gap size. The dispersion diagrams of the acoustic SSH-like unit cell for five values of the dimerization parameter δ derived from (a) the analytical model and (b) measured experimental data. Solid lines and dashed lines represent the real and imaginary parts of the Bloch-Floquet wave number q_F, respectively. The largest Bragg gap is indicated by the transparent orange zones.

B. Experimental demonstration

One active SSH-like unit cell is successfully designed, three-dimensionally printed, and assembled. The experimental AERs are off-the-shelf Vistaton FRWS 5 8-Ω drivers. Characterization of the mechanical parameters of the latter is achieved by direct measurement of the impedance following methods described by Rivet *et al.* [26] using quarter-inch PCB Piezotronics microphones and a single-point Polytec laser vibrometer for simultaneous pressure and velocity measurement, respectively. Active control is achieved with a commercial Speedgoat Performance machine equipped with an IO334 module (see Appendix B). COMSOL MULTIPHYSICS finite-element simulations are performed, enabling design optimization and experimental validation [36]. The mass, resistance, and compliance are characterized and actively tuned as summarized in Table I [36]. The goal is first to decrease the resonance frequency and second to increase the quality factor of the resonators. The former effectively increases the locally-resonant-gap and Bragg-gap frequency separation and the latter decreases system losses.

TABLE I. Impedance synthesis. The nominal/passive mechanical parameters of the AER are multiplied by the respective tuning parameters μ_M, μ_R, and μ_C to obtain the desired synthesized mechanical parameters.

	Mass	Resistance	Compliance
Nominal	5.29 g	0.297 kg/s	175 μm/N
μ_M, μ_R, μ_C	0.5	0.09	0.42
Synthesized	2.65 g	0.0267 kg/s	73.5 μm/N

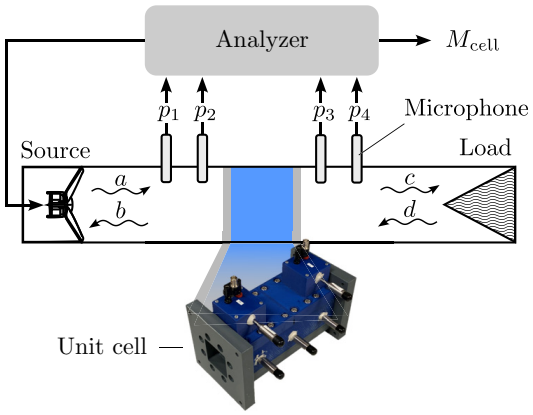

FIG. 4. Characterization of the experimental unit cell using a loaded Kundt duct and four pressure microphones. Spatial separation of the microphones on both sides of the sample allows the determination of the forward [(a),(c)] and backward [(b),(d)] complex field amplitudes and subsequently the sample transfer matrix M_{cell} via a digital analyzer.

Experimental dispersion curves are obtained with use of the aforementioned TMM. The total unit-cell transfer matrix M_{cell} is measured following the ASTM standard procedure [39], which relies on impedance-tube measurements with four microphones as shown in Fig. 4. The experimental dispersion curves are plotted in Fig. 3(b).

Remarkable consistency can be noticed throughout both the model and the experimental results, reflecting the efficacy of the proposed active control scheme. In particular, the Bragg gaps open as a function of the dimerization parameter δ. There are, however, some noticeable discrepancies around the natural resonance frequency of the resonators. Indeed, reliable feed-forward impedance synthesis demands highly accurate estimations of the AERs' mechanical parameters—this is especially relevant for the significant synthesis used here. Misestimations of these parameters can result in the synthesis of multiple-degrees-of-freedom impedances, which is perhaps made evident by an increased evanescent component $\text{Im}(q_F)$ of the wave around the local resonance in the experimental dispersion. More-accurate impedance-synthesis control schemes may be worth investigating [40,41] to mitigate these effects. That being said, this high-energy dissipation at the resonance has little, if any, effect on the Bragg gap, which is the focus of this work.

C. Topological interface states in a finite metacrystal

The topological nature of the system can be made evident by the interfacing of two topologically distinct phases of the crystal and seeking interface states. The latter will appear as a transmission peak within the aforementioned Bragg gap. An eight-cell system is modeled with use of COMSOL MULTIPHYSICS [Fig. 5(a)] for multiple coupling

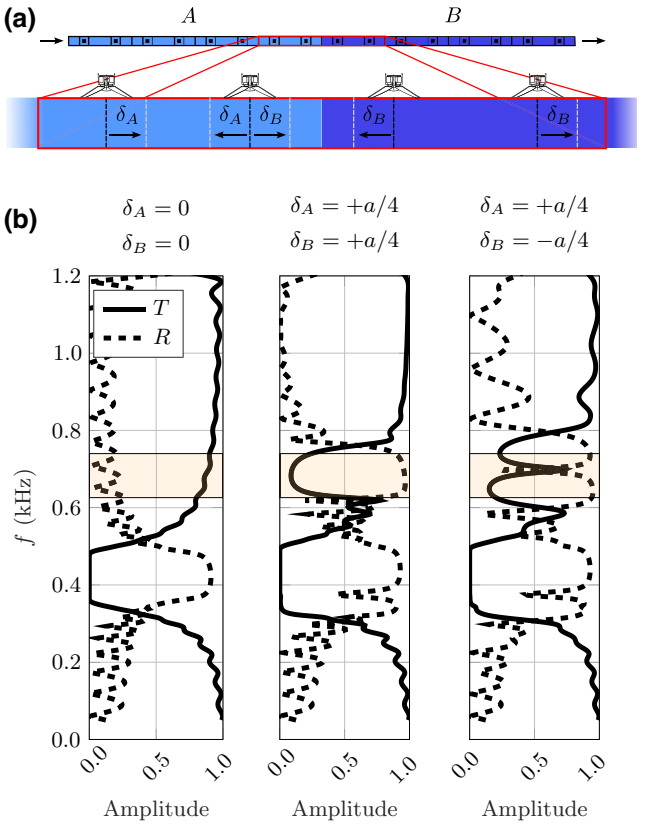

FIG. 5. Simulated topological interface states in an eight-cell active-dimer system. (a) Finite-element model of the eight-cell system with active dimers. The finite crystal is composed of two parts, labeled A and B, where the dimerization parameters are independently controlled. (b) Transmission T and reflection R as a function of frequency for different coupling configurations. The dispersion Bragg gap corresponding to $\delta = \pm a/4$ from the analytical model is indicated by the transparent orange bars.

configurations. The finite crystal is composed of two parts, labeled A and B, where the dimerization parameters, δ_A and δ_B, are independently controlled. By our setting ports at the extremities of the crystal, the scattering matrix S and consequently the transmission T and reflection R can be computed. Figure 5(b) shows R and T as a function of frequency for the following coupling configurations:

(a) $\delta_A = \delta_B = 0$. For equal coupling, the transmission is impeded only at the AER resonance frequency, effectively drawing out the locally resonant gap.

(b) $\delta_A = \delta_B = +a/4$. The dimers of both parts are uniformly coupled, resulting in an interfaceless crystal of trivial phase. As expected from the dispersion curves, the transmission drops at the Bragg gap. Furthermore, the uniform topological phase ($\delta_A = \delta_B = -a/4$) yields similar results.

(c) $\delta_A = -\delta_B = +a/4$. An interface between the trivial phase and the topological phase is created. The latter yields

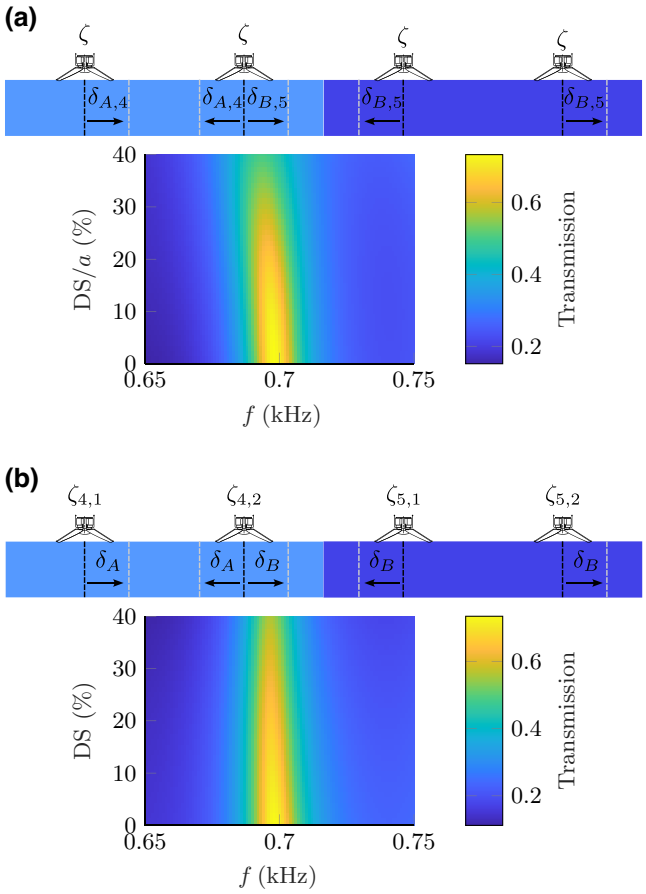

FIG. 6. Effect of defects on the topological interface state. The center transmission peak corresponding to the topological interface state is plotted as a function of the disorder strength (DS) for both (a) coupling and (b) on-site disorders. (a) All AERs along each part of the chain have identical mechanical impedances ζ and the cell couplings δ randomly (uniformly) differ from each another with strength DS. (b) The mechanical impedances ζ randomly differ and the cell couplings δ in each part are the same.

a narrow transmission peak at the center of the Bragg gap, which is indicative of a topological interface state.

The robustness of these topological states can be observed by the tracing out of the center transmission peak when coupling-parameter disorder is progressively generated in each cell. This is shown in Fig. 6(a), where the transmission peak remains almost unaffected by large disorders that do not close the band gap (up to 25% of lattice period).

D. Symmetry-protected topological interface states

Generally speaking, one-dimensional topological phases are symmetry protected, and here one may be tempted to think the protection is a direct consequence of chiral symmetry as is the case in regular tight-binding SSH chains made of evanescently coupled identical resonators. However, it is not the case for this acoustic system as the topological interface state is also robust with regard to variations in AER resonance frequencies ω_0, i.e., on-site disorder. Figure 6(b) shows the center transmission peak when we randomly shift the AER mechanical-impedance values ζ, directly related to ω_0, of every AER. In other words, the mass, resistance, and compliance of each AER are gradually shifted from their nominal values, effectively randomizing their resonance frequencies using a uniform distribution. Surprisingly, remarkable resilience of the transmission peak can be observed up to disorders exceeding 40% of the nominal impedance values ζ. Indeed, the change in ζ does not significantly alter the scattering matrix far from the local resonance at the Bragg gap where topology interface states emerge. We argue that the symmetry responsible for the topological protection in this system is that of time-reversal symmetry and equality of the far-field scattering matrices as explained in a related study by Zangeneh-Nejad and Fleury [4], albeit for a chain of passive scatterers. Their TMM-derived analytical model also produced an eigenvalue problem involving the single-cell transfer matrix M_{cell}. Here, equality of the far-field scattering matrices of the AERs is obvious as both AERs composing the unit cell are assumed to be identical. Time-reversal symmetry, on the other hand, guarantees that $M_{\text{cell}} \in \text{SU}(1,1)$, the group of non-Hermitian matrices of the form

$$M_{\text{cell}} = \begin{pmatrix} \alpha & \beta \\ \delta & \gamma \end{pmatrix} \in \text{SU}(1,1) \Rightarrow \begin{cases} \alpha - \gamma^* = 0, \\ \beta - \delta^* = 0. \end{cases} \tag{13}$$

Keeping in mind that M_{cell} is frequency dependent, we can assess a measure of the "SU(1,1)-ness" of M_{cell} by computing the standard score Z of the difference between the diagonal elements as a function of the angular frequency ω:

$$Z_{\alpha\gamma^*}(\omega) = \frac{(\alpha(\omega) - \gamma^*(\omega)) - \mu_{\alpha\gamma^*}}{\sigma_{\alpha\gamma^*}}, \tag{14}$$

$$Z_{\beta\delta^*}(\omega) = \frac{(\beta(\omega) - \delta^*(\omega)) - \mu_{\beta\delta^*}}{\sigma_{\beta\delta^*}}, \tag{15}$$

where μ and σ are the mean and standard deviations over frequency of the differences, respectively. The latter is plotted for the maximum coupling $\delta = +a/4$ for the analytical and experimental single cell in Figs. 7(a) and 7(b), respectively.

The proximity to zero is a measure of the "SU(1,1)-ness" of M_{cell}. Around the locally resonant gap (highlighted in orange), the Z score strongly diverges from the origin. This is due to the dissipative nature of the AERs, which breaks time-reversal symmetry—setting the mechanical resistance R_m to zero in the model effectively neutralizes the normalized differences throughout the whole frequency range. At the Bragg gap where, topology is relevant, the curves for both the analytical model and the experimental

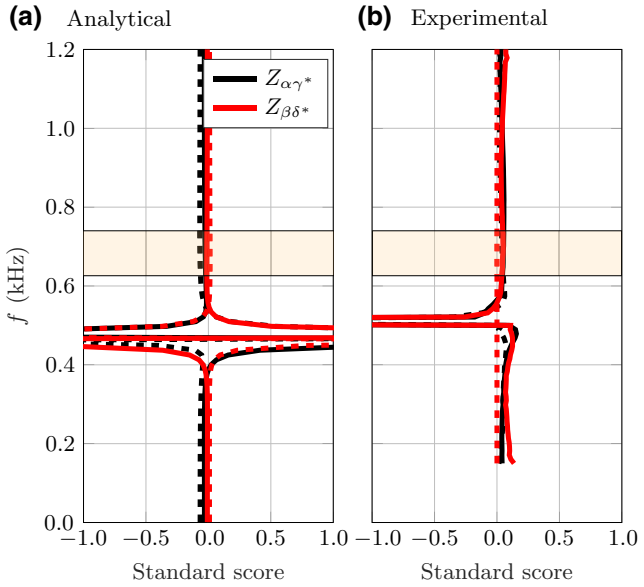

FIG. 7. Standard score Z assessing the "SU(1, 1)-ness" for the analytical model (a) and measured experimental data (b). Solid and dashed lines correspond to real and complex parts, respectively. The largest Bragg gap from the dispersion in Fig. 3(a) is indicated by the transparent orange zones.

data are much closer to the origin, which indicates that the aforementioned topological theory can be applied.

V. CONCLUSIONS

An active dimer composed of two electronically controlled AERs is presented. We demonstrate a TMM-derived analytical model and a current control scheme that enables shaping of both the locally resonant gap and the Bragg gap. One active unit cell is built and characterized by our measuring its transfer matrix and subsequently deriving the dispersion curve by applying the Bloch theorem. The proposed model yields metacrystal dispersion curves that closely match those obtained from experiments. Most notably, we show that the locally resonant gap and the Bragg gap can be easily shaped via speaker impedance synthesis and dimerization parameter tuning δ, respectively. With finite-element modeling, we showe that a finite SSH-like metacrystal composed of these active cells can host topological interface states protected by time-reversal symmetry and equality of the far-field scattering matrices. Owing to the wide tunability and reconfigurability, the presented active unit cell opens up a new path to seek novel physical phenomena such as those involving time-modulated interaction, time-reversal-symmetry breaking, or nonlinearity. For example, the latter can be achieved by simple modification of the current control scheme and can thus serve as an experimental vessel for exploring nonlinear topological systems [38].

ACKNOWLEDGMENTS

This research was supported by the Swiss National Science Foundation under Grant No. 200020_200498.

APPENDIX A: DISPERSION MEASUREMENT

The dispersion of an acoustic metacrystal can be obtained by measuring the transfer matrix of a single unit cell.

Assuming continuity of pressure and volumetric flow, let there be a stratified medium of total length a in an acoustic duct (Fig. 8). The total cell transfer matrix M_{cell} relating the left and right complex field amplitudes is given by the matrix product of each subcell composing the cell [35,42,43]:

$$M_{\text{cell}} = M_1 M_2 \cdots M_n. \tag{A1}$$

Noting $|\psi\rangle = (p_n^+, p_n^-)^T$, we find the application of the Bloch theorem with respect to the system periodicity yields the following Bloch eigenvalue problem:

$$M_{\text{cell}}(\omega)\,|\psi\rangle = e^{jq_F(\omega)a}\,|\psi\rangle\,, \tag{A2}$$

where ω is the angular frequency and q_F is the Floquet-Bloch eigenvalue. For each value of ω, $M_{\text{cell}}(\omega)$ can be diagonalized, which yields the band structure:

$$q_F(\omega) = \arccos\left(\frac{1}{2}Tr(M_{\text{cell}}(\omega))\right)/a. \tag{A3}$$

The latter holds as long as reciprocity of the system is conserved [44], or equivalently $\det M = 1$.

APPENDIX B: IMPEDANCE SYNTHESIS

Here we summarize the work reported by Rivet *et al.* [26]. Let us consider a closed-box electrodynamic loudspeaker subjected to an exogenous sound pressure p_f at the diaphragm and an electric current i at its electrical terminals as shown in Fig. 9. Assuming the steady state and expressed in the frequency domain, its velocity response

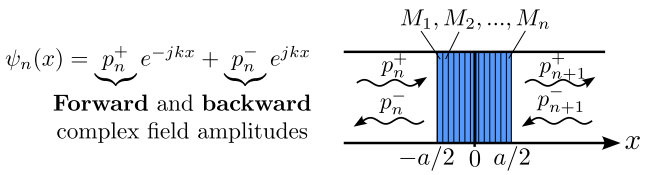

FIG. 8. Transfer-matrix method. The total cell transfer matrix M_{cell} is composed of n segments, each specified by its own transfer matrix M_n.

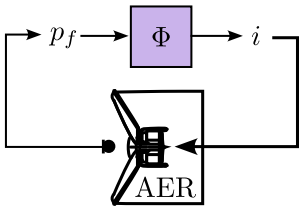

FIG. 9. Impedance-synthesis control scheme. The front pressure is measured at the front of the AER diaphragm (cross section) with a microphone and is multiplied by a transfer function Φ, which in turn outputs the drive current required to achieve a specified target impedance.

$v(s)$ is derived from Newton's second law of motion:

$$\zeta_{mc}(s)v(s) = S_d p_f(s) - B\ell i(s), \tag{B1}$$

where ζ_{mc} is the total mechanical impedance (N s/m), including the compliance of air inside the cabinet, v is the diaphragm velocity (m/s), S_d is the diaphragm surface area (m^2), p_f is the pressure in front of the diaphragm (Pa), $B\ell$ is the force factor (T m), i is the electric current (A), and $s = j\omega$ is the Laplace variable (rad/s).

This allows us to derive the electric current $i(s)$ required to achieve a target mechanical impedance ζ_{st} (Pa s/m) at the diaphragm:

$$i(s) = \frac{(\zeta_{st}(s) - \zeta_{mc}(s))v(s)}{Bl}. \tag{B2}$$

We can specify ζ_{st} to have the following form:

$$\zeta_{st}(s) = \mu_M M_{ms} s + \mu_R R_{ms} + \mu_C / C_{mc} s, \tag{B3}$$

where M_{ms} is the diaphragm mass (kg), R_{ms} is the mechanical resistance, C_{mc} is the compliance of the speaker and the cabinet (s^2/kg), and μ_M, μ_R, and μ_C are control parameters Thus, the control current required to synthesize a target virtual impedance ζ_{st} is given by

$$i(s) = p_f(s)\Phi(s), \tag{B4}$$

where

$$\Phi = \frac{S_d}{Bl} \times \left[\frac{(\mu_M - 1)M_{ms}s + (\mu_R - 1)R_{ms} + (\mu_C - 1)/C_{mc}s}{\mu_M M_{ms}s + \mu_R R_{ms} + \mu_C / C_{mc}s}\right] \tag{B5}$$

is the transfer function.

In practice, sound waves arriving at the microphones are detected, digitally sampled, and processed in real time by a software program running on a Speedgoat Performance machine equipped with an IO334 module. The digital output signals are then converted back to analog and are fed back to the speakers to generate the desired synthesized response. The Speedgoat Performance machine can reliably deliver processing delays as short as 25 μs, which enables large synthesis as explained in a recent stability study by De Bono *et al.* [45].

[1] S. He and J. D. Maynard, Detailed Measurements of Inelastic Scattering in Anderson Localization, Phys. Rev. Lett. **57**, 3171 (1986).
[2] J. D. Maynard, A possible explanation for the discrepancy in electron persistent current amplitudes: A superfluid persistent current analog, J. Low Temp. Phys. **89**, 155 (1992).
[3] M. Xiao, G. Ma, Z. Yang, P. Sheng, Z. Q. Zhang, and C. T. Chan, Geometric phase and band inversion in periodic acoustic systems, Nat. Phys. **11**, 240 (2015).
[4] F. Zangeneh-Nejad and R. Fleury, Topological analog signal processing, Nat. Commun. **10**, 1 (2019).
[5] Z. Yang and B. Zhang, Acoustic Type-II Weyl Nodes from Stacking Dimerized Chains, Phys. Rev. Lett. **117**, 1 (2016).
[6] M. Esmann, F. R. Lamberti, A. Lemaître, and N. D. Lanzillotti-Kimura, Topological acoustics in coupled nanocavity arrays, Phys. Rev. B **98**, 161109 (2018).
[7] Y. X. Shen, L. S. Zeng, Z. G. Geng, D. G. Zhao, Y. G. Peng, and X. F. Zhu, Acoustic Adiabatic Propagation Based on Topological Pumping in a Coupled Multicavity Chain Lattice, Phys. Rev. Appl. **14**, 1 (2020).
[8] M. Yan, X. Huang, L. Luo, J. Lu, W. Deng, and Z. Liu, Acoustic square-root topological states, Phys. Rev. B **102**, 180102 (2020).
[9] Z. G. Chen, L. Wang, G. Zhang, and G. Ma, Chiral Symmetry Breaking of Tight-Binding Models in Coupled Acoustic-Cavity Systems, Phys. Rev. Appl. **14**, 1 (2020).
[10] D. Zhao, X. Chen, P. Li, and X. F. Zhu, Subwavelength acoustic energy harvesting via topological interface states in 1D Helmholtz resonator arrays, AIP Adv. **11**, 015241 (2021).
[11] Y. Aurégan and V. Pagneux, PT-Symmetric Scattering in Flow Duct Acoustics, Phys. Rev. Lett. **118**, 174301 (2017).
[12] J. Christensen, M. Willatzen, V. R. Velasco, and M. H. Lu, Parity-Time Synthetic Phononic Media, Phys. Rev. Lett. **116**, 207601 (2016).
[13] R. Fleury, D. Sounas, and A. Alù, An invisible acoustic sensor based on parity-time symmetry, Nat. Commun. **6**, 1 (2015).
[14] C. Shi, M. Dubois, Y. Chen, L. Cheng, H. Ramezani, Y. Wang, and X. Zhang, Accessing the exceptional points of parity-time symmetric acoustics, Nat. Commun. **7**, 1 (2016).
[15] L. Zhang, Y. Yang, Y. Ge, Y. J. Guan, Q. Chen, Q. Yan, F. Chen, R. Xi, Y. Li, D. Jia, S. Q. Yuan, H. X. Sun, H. Chen, and B. Zhang, Acoustic non-Hermitian skin effect from twisted winding topology, Nat. Commun. **12**, 6 (2021).
[16] J. J. Liu, Z. W. Li, Z. G. Chen, W. Tang, A. Chen, B. Liang, G. Ma, and J. C. Cheng, Experimental Realization of Weyl

Exceptional Rings in a Synthetic Three-Dimensional Non-Hermitian Phononic Crystal, Phys. Rev. Lett. **129**, 084301 (2022).

[17] G. Ma and P. Sheng, Acoustic metamaterials: From local resonances to broad horizons, Sci. Adv. **2**, e1501595 (2016).

[18] B. I. Popa and S. A. Cummer, Non-reciprocal and highly nonlinear active acoustic metamaterials, Nat. Commun. **5**, 3398 (2014).

[19] N. Boechler, G. Theocharis, and C. Daraio, Bifurcation-based acoustic switching and rectification, Nat. Mater. **10**, 665 (2011).

[20] F. Zangeneh-Nejad and R. Fleury, Doppler-based acoustic gyrator, Appl. Sci. (Switzerland) **8**, 1083 (2018).

[21] B. Liang, X. S. Guo, J. Tu, D. Zhang, and J. C. Cheng, An acoustic rectifier, Nat. Mater. **9**, 989 (2010).

[22] R. Fleury, D. L. Sounas, C. F. Sieck, M. R. Haberman, and A. Alù, Sound isolation and giant linear nonreciprocity in a compact acoustic circulator, Science **343**, 516 (2014).

[23] R. Fleury, D. L. Sounas, and A. Alù, Subwavelength ultrasonic circulator based on spatiotemporal modulation, Phys. Rev. B - Condens. Matter Mater. Phys. **91**, 174306 (2015).

[24] B. I. Popa, D. Shinde, A. Konneker, and S. A. Cummer, Active acoustic metamaterials reconfigurable in real time, Phys. Rev. B - Condens. Matter Mater. Phys. **91**, 220303 (2015).

[25] C. Cho, X. Wen, N. Park, and J. Li, Digitally virtualized atoms for acoustic metamaterials, Nat. Commun. **11**, 1 (2020).

[26] E. Rivet, S. Karkar, and H. Lissek, Broadband low-frequency electroacoustic absorbers through hybrid sensor-/shunt-based impedance control, IEEE Trans. Control Syst. Technol. **25**, 10.63 (2017).

[27] E. Rivet, S. Karkar, and H. Lissek, On the optimisation of multi-degree-of-freedom acoustic impedances of low-frequency electroacoustic absorbers for room modal equalisation, Acta Acust. United Acust. **103**, 1025 (2017).

[28] R. Boulandet, H. Lissek, S. Karkar, M. Collet, G. Matten, M. Ouisse, and M. Versaevel, Duct modes damping through an adjustable electroacoustic liner under grazing incidence, J. Sound Vib. **426**, 19 (2018).

[29] E. Rivet, A. Brandstötter, K. G. Makris, H. Lissek, S. Rotter, and R. Fleury, Constant-pressure sound waves in non-Hermitian disordered media, Nat. Phys. **14**, 942 (2018).

[30] H. Lissek, E. Rivet, T. Laurence, and R. Fleury, Toward wideband steerable acoustic metasurfaces with arrays of active electroacoustic resonators, J. Appl. Phys. **123**, 091714 (2018).

[31] W. P. Su, J. R. Schrieffer, and A. J. Heeger, Solitons in Polyacetylene, Phys. Rev. Lett. **42**, 1698 (1979).

[32] A. Coutant, A. Sivadon, L. Zheng, V. Achilleos, O. Richoux, G. Theocharis, and V. Pagneux, Acoustic Su-Schrieffer-Heeger lattice: Direct mapping of acoustic waveguides to the Su-Schrieffer-Heeger model, Phys. Rev. B **103**, 1 (2021).

[33] L. Y. Zheng, V. Achilleos, O. Richoux, G. Theocharis, and V. Pagneux, Observation of Edge Waves in a Two-Dimensional Su-Schrieffer-Heeger Acoustic Network, Phys. Rev. Appl. **12**, 034014 (2019).

[34] X. Li, Y. Meng, X. Wu, S. Yan, Y. Huang, S. Wang, and W. Wen, Su-Schrieffer-Heeger model inspired acoustic interface states and edge states, Appl. Phys. Lett. **113**, 203501 (2018).

[35] O. Richoux and V. Pagneux, Acoustic characterization of the Hofstadter butterfly with resonant scatterers, Europhys. Lett. **59**, 34 (2002).

[36] See Supplemental Material at http://link.aps.org/supplemental/10.1103/PhysRevApplied.20.014022 for simulation and experimental details.

[37] S. Yves, R. Fleury, F. Lemoult, M. Fink, and G. Lerosey, Topological acoustic polaritons: Robust sound manipulation at the subwavelength scale, New J. Phys. **19**, 075003 (2017).

[38] X. Guo, H. Lissek, and R. Fleury, Improving Sound Absorption through Nonlinear Active Electroacoustic Resonators, Phys. Rev. Appl. **13**, 1 (2020).

[39] ASTM E2611-09. Standard Test Method for Measurement of Normal Incidence Sound Transmission of Acoustical Materials Based on the Transfer Matrix Method (American Society for Testing and Materials).

[40] X. Guo, M. Volery, and H. Lissek, PID-like active impedance control for electroacoustic resonators to design tunable single-degree-of-freedom sound absorbers, J. Sound Vib. **525**, 116784 (2022).

[41] M. Volery, X. Guo, and H. Lissek, Robust direct acoustic impedance control using two microphones for mixed feedforward-feedback controller, Acta Acust. **7**, 2 (2023).

[42] O. Richoux, E. Morand, and L. Simon, Analytical study of the propagation of acoustic waves in a 1D weakly disordered lattice, Ann. Phys. (N. Y) **324**, 1983 (2009).

[43] X. Wang and C. M. Mak, Acoustic performance of a duct loaded with identical resonators, J. Acoust. Soc. Am. **131**, EL316 (2012).

[44] N. Jiménez, J. P. Groby, and V. Romero-García, The transfer matrix method in acoustics: Modelling one-dimensional acoustic systems, phononic crystals and acoustic metamaterials, Top. Appl. Phys. **143**, 103 (2021).

[45] E. De Bono, M. Collet, G. Matten, S. Karkar, H. Lissek, M. Ouisse, K. Billon, T. Laurence, and M. Volery, Effect of time delay on the impedance control of a pressure-based, current-driven electroacoustic absorber, J. Sound Vib. **537**, 117201 (2022).